Journal of Alloys and Compounds 656 (2016) 5–12

Contents lists available at ScienceDirect

Journal of Alloys and Compounds

journal homepage: http://www.elsevier.com/locate/jalcom

Effect of Sm^{3+}–Gd^{3+} on structural, electrical and magnetic properties of Mn–Zn ferrites synthesized via combustion route

V. Jagadeesha Angadi [a], B. Rudraswamy [a], K. Sadhana [b], S.Ramana Murthy [b], K. Praveena [c, d, *]

[a] Department of Physics, Bangalore University, Bangalore 560056, India
[b] Department of Physics, University College of Science, Osmania University, Saifabad, Hyderabad 500 004, India
[c] Materials Research Centre, Indian Institute of Science, Bangalore 560012, India
[d] School of Physics, Eternal University, Baru Sahib 173101, Himachal Pradesh, India

ARTICLE INFO

Article history:
Received 1 July 2015
Received in revised form
8 September 2015
Accepted 25 September 2015
Available online xxx

Keywords:
Ferrites
Dielectric properties
Magnetic properties
Y–K angle
Electron paramagnetic resonance

ABSTRACT

Nanocrystalline $Mn_{0.4}$ $Zn_{0.6}$ $Sm_xGd_yFe_{2-(x+y)}O_4$ ($x = y = 0.01$, 0.02, 0.03, 0.04 and 0.05) were synthesized by combustion route. The detailed structural studies were carried out through X-ray diffractometer (XRD), Fourier transform infrared spectroscopy (FTIR), transmission electron microscopy (TEM). The results confirms the formation of mixed spine phase with cubic structure due to the distortion created with co-dopants substitution at Fe site in Mn–Zn ferrite lattice. Further, the crystallite size increases with an increase of Sm^{3+}–Gd^{3+} ions concentration while lattice parameter and lattice strain decreases. Furthermore, the effect of Sm–Gd co-doping in Mn–Zn ferrite on the room temperature electrical (dielectric studies) studies were carried out in the wide frequency range 1 GHz–5 GHz. The magnetic studies were carried out using vibrating sample magnetometer (VSM) under applied magnetic field of 1.5T and also room temperature electron paramagnetic resonance (EPR) spectra's were recorded. From the results of dielectric studies, it shows that the real and imaginary part of permittivities are increasing with variation of Gd^{3+} and Sm^{3+} concentration. The magnetic studies reveal the decrease of remnant, saturation magnetization and coercivity with increasing of Sm^{3+}–Gd^{3+} ion concentration. The *g*-value, peak-to-peak line width and spin concentration evaluated from EPR spectra correlated with cations occupancy. The electromagnetic properties clearly indicate that these materials are the good candidates which are useful at L and C band frequency.

1. Introduction

The remarkable properties of rare earth substituted Mn–Zn ferrites having a high resistivity, high saturation magnetization, low loss and high initial permeability, these properties are useful for low and high frequency applications such as transformer core, multilayered chip inductors, information storage system, ferrofluid applications, magneto caloric refrigeration and magnetic diagnostics [1–3]. A small amount of rare earth ion substituted at Fe^{3+}site in ferrites have shown appreciable enhancement in both electrical as well as magnetic properties due to the rare earth ions have unpaired 4*f* electrons with strong spin orbit coupling. The substitution of rare earth ions at Fe^{3+} site will exhibit 4*f*-3*d* coupling, which helpful to determine magneto-crystalline anisotropy of the material. Hence it is possible to obtain good magnetic materials, which are useful for low and high frequency applications [4]. In particular, the rare earth ion doped Mn–Zn ferrites are favourable for magnetic properties. Due to the stable valence (3+) of rare earth ions and larger ionic radii, these dopants are the best substitutions at Fe site in Mn–Zn ferrite in order to enhance the structural, electrical and magnetic properties. Among all rare earth elements, Gd^{3+} and Sm^{3+} are good magnetic ions, which preferably substitutes at the B-site (Fe-site), as a result the magnetic parameters such as saturation magnetization deceases with increasing rare earth concentration at Fe^{3+}site because of its paramagnetic behaviour at room temperature [5]. Furthermore, the effect of different rare earth ions substituted Mn–Zn ferrites have already reported by several researchers.

* Corresponding author. Materials Research Centre, Indian Institute of Science, Bangalore 560012, India.
E-mail addresses: praveena@mrc.iisc.ernet.in, praveenaou@gmail.com (K. Praveena).

http://dx.doi.org/10.1016/j.jallcom.2015.09.222
0925-8388/

The effect of Sm doped Mn–Zn ferrites and Gd doped Mn–Zn ferrites on the magnetic and electrical properties have been studied extensively. It is well known that, high saturation magnetization, high permeability and low coercivity indeed required for an industrial application in the field of high frequency applications. It is reported that, the high magnetization and coercivity in case of Sm doped Mn–Zn ferrites and low magnetization and low coercivity in case of Gd doped Mn–Zn ferrites [6]. Hence in the current investigation, we intend to study the effect of Sm–Gd co-doped Mn–Zn ferrites on the magnetic and electrical properties towards high frequency range. In addition, the synthesis Sm^{3+}–Gd^{3+} ion doped at Fe^{3+} site in Mn–Zn ferrites have not yet been reported in the literature. There are many conventional synthesis methods to synthesize rare earth ion doped Mn–Zn ferrites such as chemical co-precipitation method [7–9], solid state [10], hydrothermal synthesis [11], microwave hydrothermal (M–H) [12], sol–gel [13,14] and solution combustion [15,16]. Among all, solution combustion route is simple and economically feasible [17] to obtain nanosized Sm^{3+}–Gd^{3+} co doped Mn–Zn ferrite particles at its as-synthesized form without need of post heat treatment. In addition, this method is simple, short reaction time and inexpensive, which allows the production of fine, homogeneous crystalline powders at its as-prepared form. In the present investigation, the detailed investigation on the effect of Sm and Gd co-doping on the structural, electrical and magnetic properties of Mn–Zn ferrites have been taken up and correlation between the electrical and magnetic properties of the synthesized materials are reported.

2. Experimental

The Sm^{3+}-Gd^{3+}codoped $Mn_{0.4}Zn_{0.6}Sm_xGd_yFe_{2-(x+y)}O_4$ (where, x = y = 0.01, 0.02, 0.03, 0.04 and 0.05) were synthesized by solution combustion route using mixture of glucose and urea as a fuel. The stiochiometric amounts of manganese nitrate [Mn $(NO_3)_2.4H_2O$], zinc nitrate hexahydrate [Zn $(NO_3)_2.6H_2O$], and iron nitrate nanohydrous [Fe $(NO_3)_3.9H_2O$], Samarium nitrate [$Sm(NO_3)_2$] and Gadolinium [Gd $(NO_3)_2$] are as oxidizers and urea [NH_2CONH_2] and glucose [$C_6H_{12}O_6$] as fuels. Considering the complete combustion reaction, the mixture of both fuels were taken, such that, the oxidizer to fuel ratio to be unity using the oxidizing the reducing valencies of metal nitrates and fuels. The stoichiometric amounts of the metal nitrates and fuels were dissolved with 30 ml double distilled water and thoroughly stirred on the magnetic stirrer at a static spinning speed of 800 rpm for 1 h until clear transparent solution. This clear transparent solution is called redox mixture. The redox mixture was then taken in a 250 ml borosil beaker and kept in a pre-heated muffle furnace at 450 °C. Initially, the solution boils then froths and ignites to yield fine ash. The final as was then ground in agate pestle mortar and collected. To mention, the whole combustion process has gets completed in less than 20 min, whereas the reaction time of the actual ignition/flaming was few seconds.

3. Characterization techniques

The synthesized powder were characterized by X-ray diffraction make use of Panalytical X'Pert Pro MPD with CuK_α radiation of wavelength, λ = 1.5406 Å. The data was recorded in the 10–80° (2θ range) with step size of 0.02°. The structural and compositional details of the phases in each sample were extracted by Rietveld refinement on the XRD data. The Rietveld refinement was performed using the program "FullProf" [18].

The Crystallite size and strain were calculated using Williamson–Hall equation [19,20].

$$\beta \mathrm{Cos}\theta = k\lambda/D + 4\varepsilon\ \mathrm{Sin}\theta \quad (1)$$

where, β is the observed FWHM, θ is the Bragg angle, k is the Scherer's constant, λ is the wavelength of the X-ray used, D is the crystallite size, ε is the strain present in the crystal [20]. The lattice parameters, scale factor, full width at half maximum (FWHM) of then Bragg reflections were refined. The quality of fit to the observed XRD patterns were assessed by the Rietveld agreement (reliability) factors: R-pattern factor (R_p), R-weighted pattern factor (R_{wp}), R-expected (R_{exp}) and χ^2 [20]. The hoping length is calculated by Eq. (2) this is helpful to identify the distance between magnetic ions in octahedral and tetrahedral sites [21].

$$L_A = a\frac{\sqrt{3}}{4} \& L_B = a\frac{\sqrt{2}}{4} \quad (2)$$

where *a* is lattice constant.

From the FTIR spectroscopy we can find the information about the position of ions in the crystal and about the inter atomic vibration modes of the samples using Agilent FTIR spectra. The particle size and morphology of the samples were determined using transmission electron microscope (TEM), high resolution transmission electron microscope (HRTEM) JEOL, Japan. The room temperature dielectric properties such as real and imaginary part of permittivity (ε′ and ε″) were undertaken in the wide frequency range 1 GHz–5 GHz using Agilent E4991A RF Impedance/Material Analyser. The room temperature magnetization measurement was carried out by 14 TPPMS vibrating sample magnetometer (VSM) mounted on an electromagnet with a bipolar source of maximum applied field of 20 kOe.The value of anisotropy constant(K), remanence ratio S (M_r/M_s), magneton number(η_B) and Yafet-Kittel angle($\alpha_{y\text{-}k}$) were calculated using equations Eq. (3), Eq. (4), Eq. (5) and Eq. (6) respectively [22].

$$\text{Magneton number}: \quad \eta_B = M_B cos\alpha_{Y-K} M_A \quad (3)$$

$$\text{Yafet} - \text{Kittel angle}: \quad \alpha_{Y-K} = cos^{-1}\left[\frac{\eta_B - M_A}{M_B}\right] \quad (4)$$

where H_c is coercive field, M_s is saturation magnetization, M_r is remnant magnetization, S is a measure of squareness of the hysteresis loop, M_A and M_B are the magnetic moments of metal ions.

4. Results and discussion

4.1. Structural analysis by X-ray diffractometer

The XRD patterns of as-synthesized $Mn_{0.4}Zn_{0.6}Sm_xGd_yFe_{2-(x+y)}O_4$ (where, x = y = 0.01, 0.02, 0.03, 0.04 and 0.05) nanoparticles are depicted in the Fig. 1(a). It is evidenced from Fig. 1(b) that, the formation of polycrystalline, mixed spinel cubic structure. Major number of the prominent(strongest) crystal reflections at 2θ values of 18.2°, 29.88°, 35.22°, 36.72°, 42.71°, 53.03°, 56.37°, 62.03°, 73.20°, 74.53°, 86.02° and 88.70° are indexed to the Mn–Zn ferrite crystal system belongs to space group $Fd\bar{3}\ m$ (JCPDS No. 74-2400). From the XRD patterns mixed (impurity) phases are identified as Fe_2O_3, $SmFeO_3$ and $GdFeO_3$ and the amount of these residual phases (impurity phases of Fe_2O_3, $SmFeO_3$ and $GdFeO_3$ are comparatively less. In detail, the peaks at 2θ values of 24.05°, 33.05°, 40.88° and 43.37°) are indexed to the Fe_2O_3 (JCPDS No. 39-1346). With increasing Sm–Gd concentration, the peaks at 2θ values of 22.88°, 25.72°, 31.55°, 32.71°, 46.87°, 59.37° and64.03° are indexed to the formation of $SmFeO_3$ phase (JCPDS No. 74-1474) and the peaks at 2θ values of 46.87°, 49.11°, 54.04°, 59.37° and 70.30°

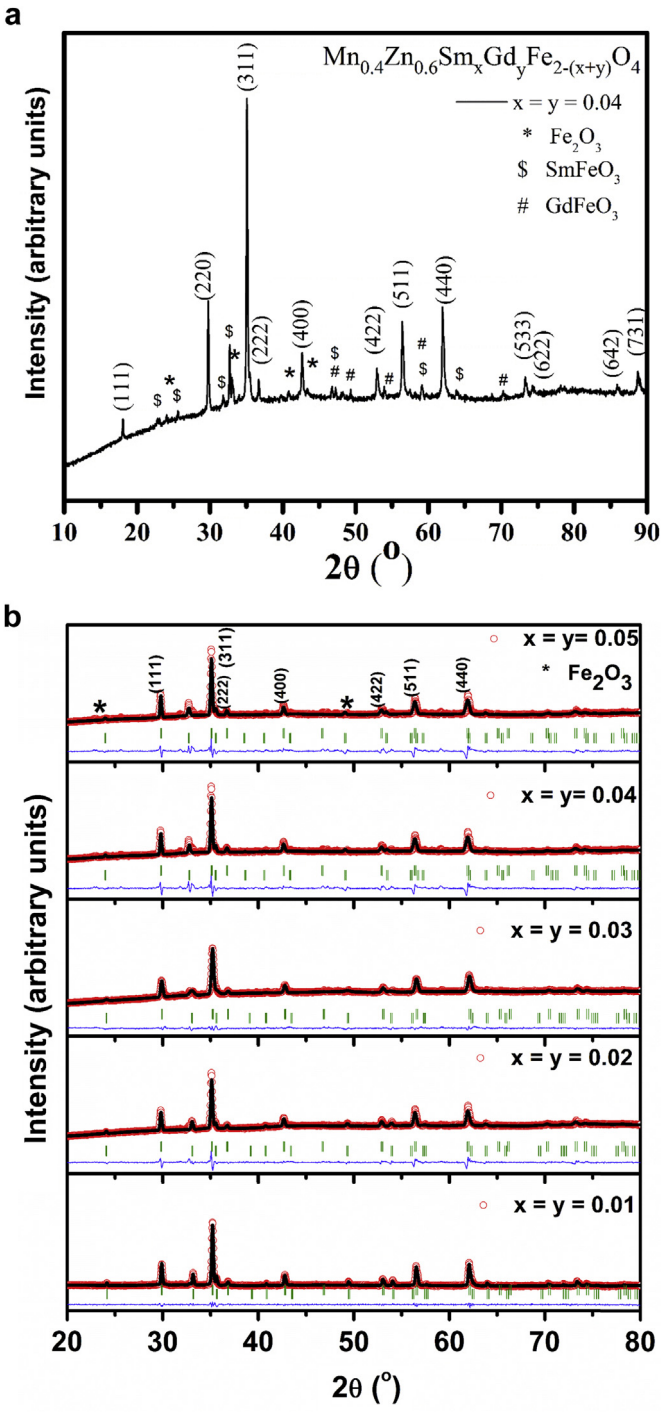

Fig. 1. (a). XRD patterns for as-synthesized $Mn_{0.4}Zn_{0.6}$ $Sm_{0.04}$ $Gd_{0.04}$ $Fe_{1.92}O_4$. b. Rietveld refined XRD patterns for as synthesized $Mn_{0.4}Zn_{0.6}$ Sm_x $Gd_yFe_{2-(x+y)}O_4$ (x = y = 0.01, 0.02, 0.03, 0.04 and 0.05).

are indexed to the formation of $GdFeO_3$ phase (JCPDS No. 78-0451). The formation of impurity phases could be due to the distortions created during the simultaneous substitution of Sm and Gd at Fe site in Mn–Zn ferrite due to the larger ionic radii of Sm (0.96 Å) and Gd (1.13 Å) compared to Fe (0.64 Å). As a result, all the peaks are shifted to the higher 2θ side as compared with the JCPDS of Mn–Zn ferrite.

The Rietveld fitted XRD patterns of as prepared $Mn_{0.4}Zn_{0.6}Sm_x$ $Gd_yFe_{2-(x+y)}O_4$ (where, x = y = 0.01, 0.02, 0.03, 0.04 and 0.05) are depicted in the Fig. 1(b). All the samples show cubic spinel structure with the space group $Fd\bar{3}\ m$. And also confirms the formation of impurity phases. From the refinement the value of lattice constant (a) unit cell volume (Å^3), R-factor values such as (R_{exp}), Bragg value (R_{Bragg}) and discrepancy factor (R_{wp}) and goodness of fit index (x^2) are shown in Table 1. It is observed that, the lattice parameters are found to increase with increasing Sm^{3+}–Gd^{3+} concentration, which is attributed to the fact that the ionic radii of Fe^{3+} smaller than that of $Sm^{3+}$and Gd^{3+}. This observation can be explained on the basis of when we consider the occupancy of cations in the interstitials of the spinel. The Variation in crystallite size (D) and strain were determined using Williamson–Hall Eq. (1) [19] and are tabulated in Table 1. The value of average crystallite size is found to decrease from 44.2 to 40.0 nm with increasing Sm^{3+}–Gd^{3+} concentration (Table 1). Further, the distances between the magnetic ions at tetrahedral (A) and octahedral (B) sites were calculated by using the Eq. (2). The hopping length of L_A and L_B decreases with increasing Sm^{3+}–Gd^{3+} concentration. This is due to fact that Fe^{3+} ions are replaced by the relative number of Sm^{3+}–Gd^{3+} ion in B site. The variation of hopping length of tetrahedral site (L_A) and octahedral site (L_B) is as shown in Table 1.

4.2. FTIR analysis

Fig. 2 shows FTIR spectra of all the samples with composition x = y = 0.01, 0.02, 0.03, 0.04 and 0.05. The position of ions in the crystal and vibrational modes has been observed in Infrared spectra [23]. The assigned peak positions are tabulated in Table 2. FTIR spectra of all the samples have observed three prominent absorption bands such as, ν_1 was found to 529–537 cm^{-1} it is attributed to tetrahedral complexes, ν_2 was found to 378–380 cm^{-1} it is assigned to octahedral complexes and ν_3 is around 350–358 cm^{-1} attribute divalent octahedral metal ion – oxygen complex. From the absorption band ν_1, shows the tetrahedral complexes and does not show any shoulders, hence the possibility of Fe^{2+} ions at A-sites is ruled out. But the octahedral complexes is an evidence of mere splitting on the absorption band found at 357 cm^{-1} and 380 cm^{-1} respectively. This is attributed to John teller distortion produced by Fe, Sm and Gd ions on B-sites in oxide state which also confirms by XRD. The difference between absorption bands $\nu_1$and ν_2 is due to changes in bond length (Fe^{3+}-O^{2-}) at tetrahedral and octahedral sites [24]. Here we can observe slight change in band position in ν_1 and ν_2 this difference is due to the method of preparation, grain size and porosity can influence in locating the band position [25,26]. The difference between the spectra upon increasing the amount of dopant elements this is may be due to the increase of the amount of undesired Fe, Gd and Sm oxides in material. On simultaneous substitution of Sm^{3+}–Gd^{3+} content, ν_1 continued to be widen is attributed to atomic mass and volume of the dopant, which affect Fe–O distances on octahedral sites, suggesting that Sm^{3+}–Gd^{3+} ions both are occupies octahedral lattice sites. The shift occur in absorption bands ν_1 and ν_2 for each octahedral and tetrahedral site due to the perturbation occurring in the Fe^{3+}- O^{2-} bond by introducing Sm^{3+} and Gd^{3+} [27].

4.3. TEM analysis

The TEM micrograph of samples with Sm^{3+}–Gd^{3+} content is shown in Fig. 3. It is clear that the particles are spherical in shape and slight agglomeration. This agglomeration can be attributed to magnetic interaction arising among ferrite nanoparticles. The particle size (DT) calculated from TEM is higher than the crystal size estimated from XRD. The addition of Sm^{3+}–Gd^{3+} reduces grain boundaries which in turn hamper its motion [28]. The selected area of electron diffraction patterns of all the samples shows spotty

Table 1
Lattice parameter (A), crystallite size (Dr), particle size (t) and Hoping lengths octahedral site ((L_A) and tetrahedral site (L_B)) and Reliability factors.

x = y	Lattice constant (a) Å	D_T nm (XRD)	Particle size nm (TEM)	Strain (%)	L_A Å	L_B Å	R_{wp}	R_p	R_{exp}	χ^2
0.01	8.45228	44.2	30.2	0.5	3.643	2.9741	7.98	10.5	2.66	1.0
0.02	8.45234	43.2	28.5	0.48	3.645	2.9756	1.36	2.27	0.82	7.5
0.03	8.45253	41.7	25.3	0.4	3.654	2.9831	1.09	1.46	0.80	3.1
0.04	8.47760	40.9	20.7	0.32	3.656	2.9845	1.70	2.83	0.80	2.4
0.05	8.47864	40.0	18.3	0.28	3.657	2.9857	1.70	2.76	0.80	1.8

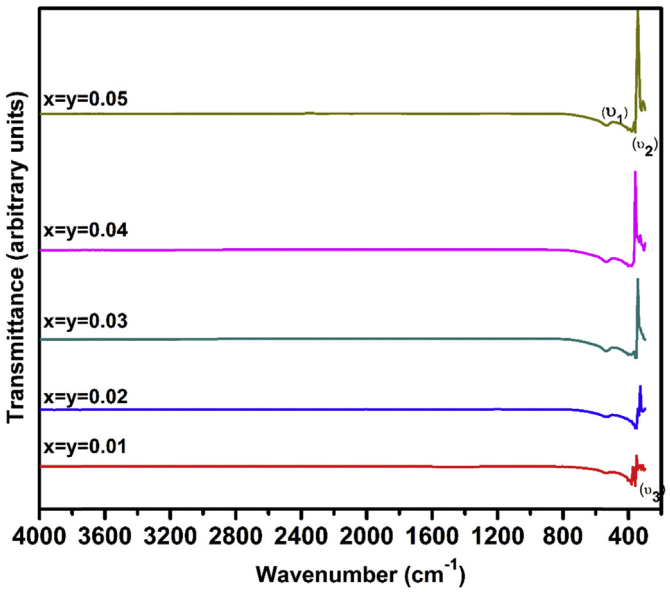

Fig. 2. FTIR spectra of $Mn_{0.4}Zn_{0.6}Sm_xGd_y\ Fe_{2-(x+y)}O_4$ (x = y = 0.01, 0.02, 0.03, 0.04 and 0.05).

Table 2
List of peak positions with composition form FTIR analysis.

Composition	Peak positions (cm^{-1})		
	υ_1	υ_2	υ_3
x = y = 0.01	537	380	358
x = y = 0.02	529	378	350
x = y = 0.03	537	387	358
x = y = 0.04	537	380	335
x = y = 0.05	529	380	358

circular ring patterns without any additional diffraction spots and rings of secondary phases revealing their crystalline spinel structure. This feature indicates the samples are highly crystalline in nature. The particle size distribution is obtained (Fig. 4) by analysing 6 TEM images for each sample. We notice that the particle size distribution follows a log-normal distribution.

4.4. Dielectric properties

The real parts of permittivity symbolize the storage capability of electric and magnetic energy and imaginary parts of permittivity represent the loss of electric and magnetic energy [29]. The frequency dependence of real and imaginary part of permittivity (ε' and ε'') at room temperature for all samples over the G-band frequency range from 1 GHz to 5 GHz are shown in Fig. 5(a). The plots show that, the dielectric constant of all the samples remains fairly constant over the frequency range (1 GHz–5 GHz) of study. The maximum value of dielectric constant 9.25 is observed form the sample x = y = 0.05 at higher concentration of Sm–Gd ions. The high frequency dielectric constants are mainly contributed by the electronic polarizations [30]. The high value of dielectric constant (ε') of the sample can be explained on the basis of hoping conduction between $Fe^{3+} \leftrightarrow Fe^{2+}$, $Mn^{2+} \leftrightarrow Mn^{3+}$, $Zn^{2+} \leftrightarrow Zn^{3+}$, Sm^{2+}–Sm^{3+}, Gd^{2+}–Gd^{3+} pairs of ions so that the dipoles align themselves in response to the alternating field [31]. The increase in number of Sm^{3+}–Gd^{3+} ions causes an increase in dielectric constant. This is because frequency of the dielectric constant in ferrites is always related with the number of Fe^{2+} ions since they are easily polarized than Fe^{3+} ions. In ferrites with spinel structure having a structural formula, $Fe^{3+}[Mn^{2+}Zn^{2+}Fe^{3+}]O_4$, Mn^{2+} and Zn^{2+} together with half of the iron ions (Fe^{3+}) occupy the B site and the remaining half of the iron ions reside in the A site. The presence of Mn^{2+}–Mn^{3+} and Zn^{2+}–Zn^{3+} gives rise to the p-type carriers (holes) whereas Fe^{2+}, Fe^{3+} Sm^{3+} and Gd^{3+} ions produce n-type carriers (electrons) [32]. Therefore, both the electrons and holes that are present in the B sites are due to the presence of the Mn, Zn, Fe, Sm and Gd ions. Since only the iron ions are present at A sites, electrons are the carriers at A sites. The distance between the ions at A sites is larger than the distance between the ions at B site. Also, the degree of co-valency for the A site ions is higher than that of the B site ions. Iwauchi [33] have established a theory of strong correlation between the conduction mechanism and dielectric behaviour of ferrites. The polarization decreases with increase in frequency and reaches a constant value due to the fact that beyond a certain frequency of external field the electron exchange $Fe^{3+} \leftrightarrow Fe^{2+}$ cannot follow the alternating field.

Fig. 5(b) shows the frequency dependence of imaginary part of permittivity (ε''). The dielectric loss represents the energy dissipation in a dielectric. The dielectric losses in ferrites cause due to the electron hopping between the Fe^{3+} to Fe^{2+}, Sm^{3+}–Fe^{3+} and Gd^{3+}- Fe^{3+} ions [34]. In the present study it was found that the imaginary permittivity remains constant in frequency range 1–5 GHz this is due to the polarization lagging behind the applied alternating electric field.

4.5. Magnetic properties

The room temperature magnetization measurements were carried out by "PPMS-14T" vibrating sample magnetometer (VSM) as shown in Fig. 6. The saturation magnetizations (M_S) of all the samples were estimated from the intercepts of a straight line extrapolated from high applied field region of the magnetization curve, with the magnetization axis. In the M–H loop it can be observed that very narrow hysteresis loops, reveals the behaviour of soft magnetic material. These features indicate the presence of super paramagnetic and single-domain particles for each of these ferrites [35]. The values of saturation magnetization (M_S) is decreasing with increasing Sm^{3+}–Gd^{3+} ion concentration this is due to the magnetic moment of Sm^{3+}–Gd^{3+} is predominantly due to the 4*f* electrons and their magnetic dipolar orientation exhibits disorder form at room temperature [36]. As Gd has the highest magnetic ordering among all the rare earth elements. The saturation moment of Gd is 7.55 μ_B per atom, i.e. there is an additional

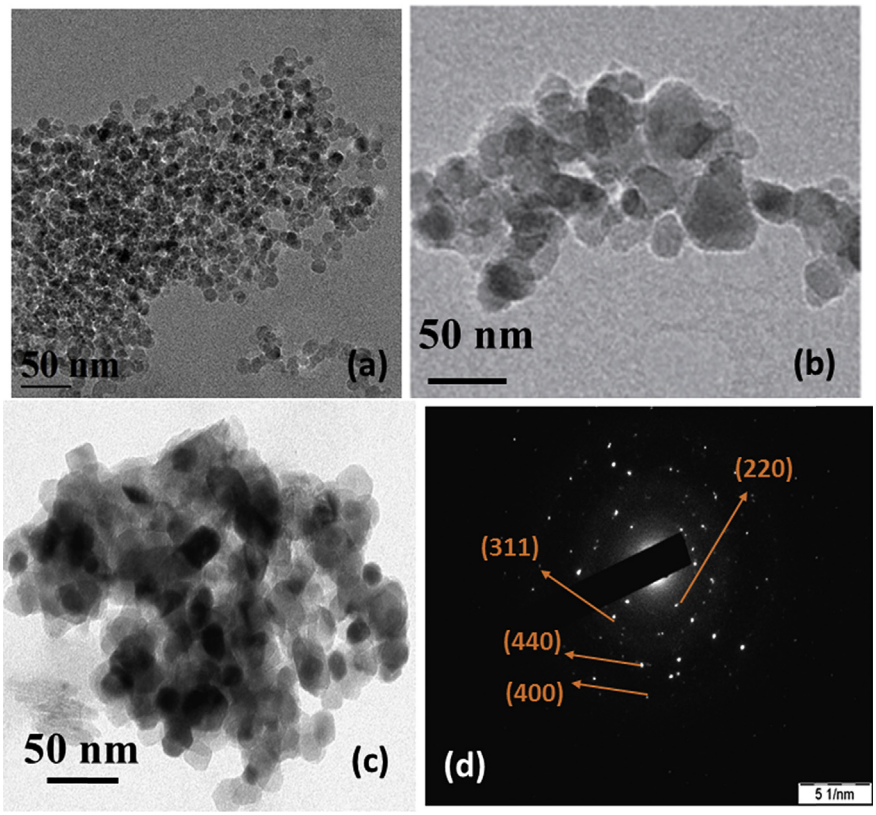

Fig. 3. TEM images of $Mn_{0.4}Zn_{0.6}Sm_xGd_yFe_{2-(x+y)}O_4$ where (a)x = y = 0.01 (b) x = y = 0.03 (c) x = y = 0.05 (d) x = y = 0.01.

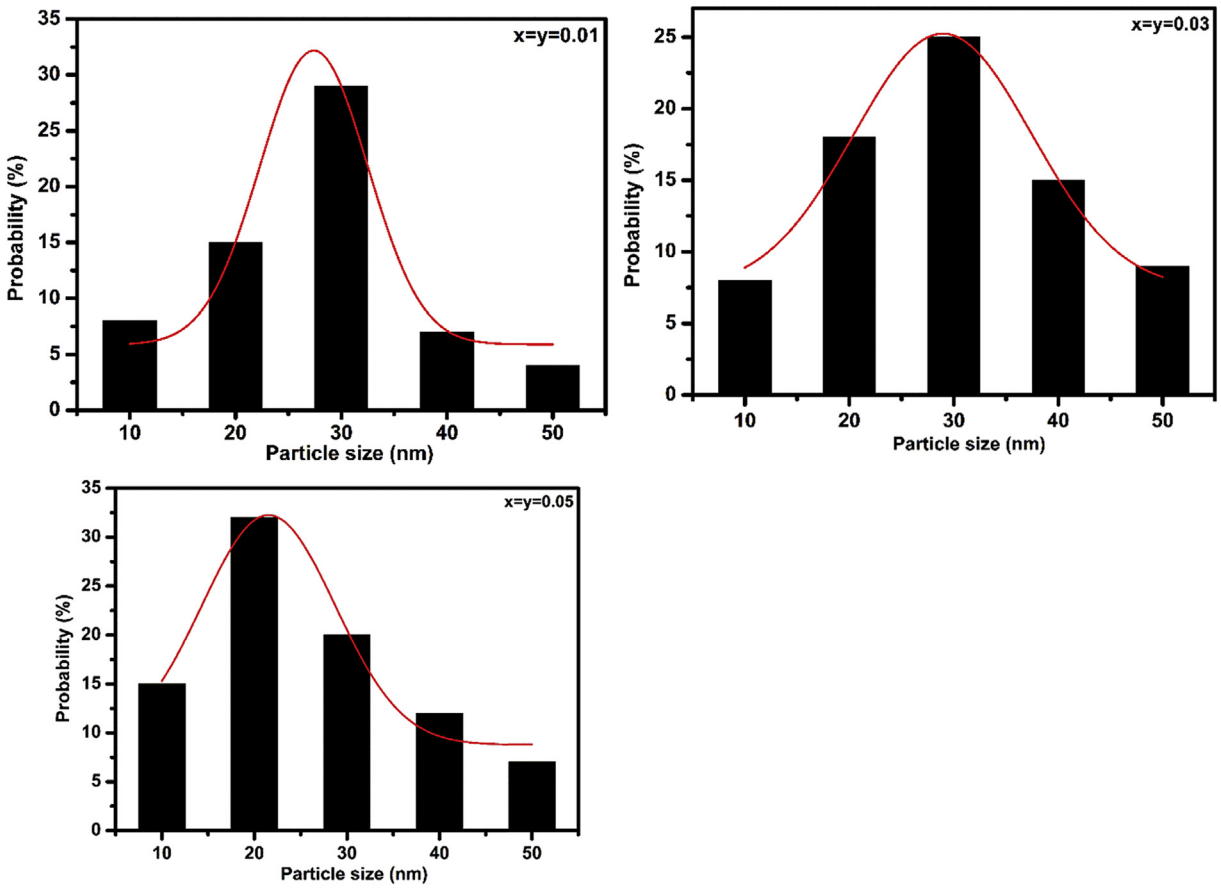

Fig. 4. Particle size distribution histograms of $Mn_{0.4}Zn_{0.6}Sm_xGd_yFe_{2-(x+y)}O_4$ where x = y = 0.01, 0.03 and 0.05.

moment of 0.55 μ_B corresponds to local 4*f* moments with S = 7/2. This additional moment is usually attributed to conduction-electron polarization. And Fe has 5 μ_B. Hence the substitution of Sm^{3+}–Gd^{3+} ion at Fe^{3+} site which reduces exchange interaction between A and B site get lower. The substituted Sm^{3+}–Gd^{3+} ions occupy the B site resulting in weaker Sm–Fe and Gd–Fe interaction as compared to the stronger Fe–Fe super-exchange interaction which leads to decrease to the saturation magnetization (M_s). The M_s is decreases with decreasing particle size, according to stochastic model the variation of magnetic properties with particle size for magnetic nanoparticle were developed by Chakraverty and Bandyopadhy [37]. According to Neel's two sub-lattice model of ferrimagnetism, the net moment is given by the formula $\mu_B = M_B(x) - M_A(x)$, where M_A and M_B are the A and B sub-lattice magnetic moments in μ_B [38]. The remnant magnetization (M_r) value estimated by the intercept of M–H loop on the magnetization axis. Reduced remnant is a measure of the squareness of the hysteresis loop and is calculated by make use of M_r and $M_{s,}$ i.e

$$S = \frac{M_r}{M_S} \tag{5}$$

where M_r and $M_s$are the remnant and saturation magnetizations, respectively. The value of S is decreasing with increasing Sm–Gd concentration. According to the Stoner-Wohlfarth model for non-interacting 3D-random ferromagnetic particles, the reduced remanence is given by $\boldsymbol{S} = 0.5$ for uniaxial anisotropy and S = 0.832 for cubic anisotropy [39]. In our samples, it is 0.55 and 0.70, which suggests that the particles are not interacting strongly and the observed anisotropy is of the cubic anisotropy type. Hence we have taken the following equation calculation of anisotropy constant (K).

$$\mathrm{K} = \frac{Hc \times Ms}{0.64} \tag{6}$$

The calculated value of anisotropy constant (K) was found to increase with increasing Sm–Gd concentration. The variation of anisotropy with respect to Sm^{3+} ion is explained on the basis of particle size with the decrease of particle size the surface to volume ratio increases and surface effect may induced a spin disorder in surface layer cause the anisotropy is increase with increase of Sm^{3+}–Gd^{3+} content. In ferrites, the coercive force obtained by reversal of the directions of the wall movement and that of domain rotation on reversing the direction of the applied magnetic field. Generally, the effective pinning for domain wall causes the coercivity; it is known that the larger grain size decreases H_C. In the present investigation, the coercive values are increasing with increasing Sm^{3+}–Gd^{3+} concentration; hence probability of domain rotation is also high. The materials with lower grain size have been used to achieve high core loss [40]. The variation of the coercivity and particle size with increasing Sm^{3+}–Gd^{3+} concentration is observed that the value of coercivity is increasing with increasing Sm^{3+}–Gd^{3+} content. The variation of particle size with H_c can be explained on the basis of domain structure and anisotropy of the crystal. Coercivity is increasing with Sm^{3+}–Gd^{3+} ion concentration is due to an increased magneto crystalline anisotropy resulting from the coupling of the spin of the Mn^{2+},Zn^{2+},Sm^{3+},Gd^{3+} and Fe^{3+} ions. The magnetic moment (n_B) is calculated using $\eta_B = M_B cos\alpha_{Y-K} M_A$ .where M_A and M_B are the magnetic moment of an metal ions. The value of η_B strongly decreases with increasing the Sm–Gd content, which suggests that the obtained M_s values cannot be explained by assuming Néel's two sub-lattice model for ferrimagnetism. According to Néel's two sub-lattice model of ferrimagnetism, the net magnetic moment is given by the formula $\mu_{B\ (eff)} = M_B(x) - M_A(x)$, where M_A and M_B are the A and B sub-

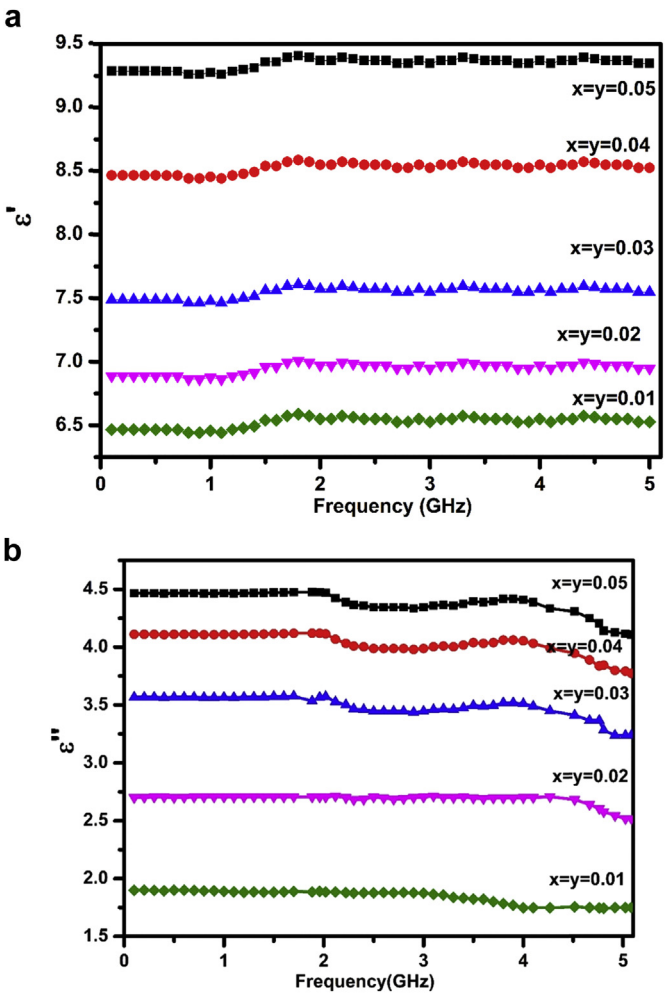

Fig. 5. (a) Real part of permittivity (ε′) of $Mn_{0.4}Zn_{0.6}Sm_xGd_yFe_{2-(x+y)}O_4$ (x = y = 0.01, 0.02, 0.03, 0.04 and 0.05). (b) Imaginary part of permittivity (ε″) of $Mn_{0.4}Zn_{0.6}Sm_xGd_yFe_{2-(x+y)}O_4$ (x = y = 0.01, 0.02, 0.03, 0.04 and 0.05).

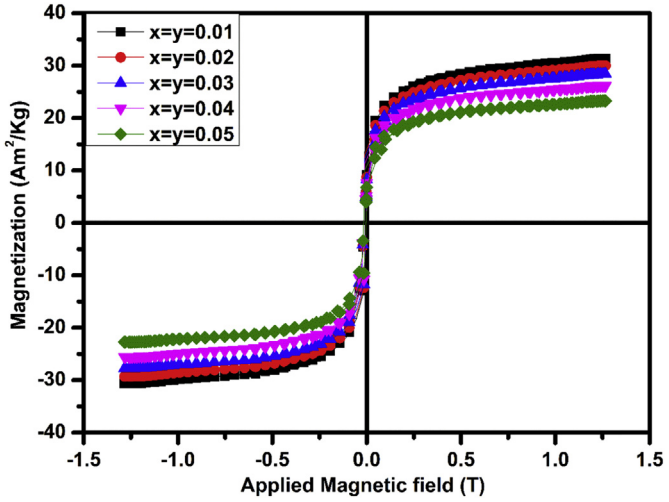

Fig. 6. Magnetic hysteresis loop for $Mn_{0.4}Zn_{0.6}Sm_xGd_yFe_{2-(x+y)}$ O_4 samples with (x = y = 0.01, 0.02, 0.03, 0.04 and 0.05).

Table 3
Saturation magnetization (M_S), remanence (M_r), reduced remanence (M_r/M_s), coercivity (H_c), magneton number (η_B), anisotropy constant (K), and Y–K angle ($\alpha_{Y\text{-}K}$) with different Sm^{3+}–Gd^{3+} concentration.

x = y	M_s (Am^2/Kg)	M_r (Am^2/Kg)	H_c (T)	M_r/M_s	n_B μ_B	K erg/Oe	$\alpha_{Y\text{-}K}$ (°)	g value
0.01	31.368	14.63	0.01641	0.4664	1.3413	0.7891	67.98	2.27
0.02	29.99	13.93	0.01628	0.46449	1.29292	0.76381	68.92	2.15
0.03	28.41	13.12	0.01642	0.46181	1.23478	0.71025	72.49	2.01
0.04	26.18	12.10	0.01629	0.46218	1.14706	0.66268	74.21	1.98
0.05	23.23	10.77	0.01643	0.46362	1.02597	0.58075	75.98	1.92

lattice magnetic moments in μ_B [41] and also the calculated value of n_B goes on decreases with increasing sm^{3+}–Gd^{3+} ion it is clear that the existence of on effectively uniaxial anisotropy in magnetic particle. The degree of spin canting effect is explained with the help of Yafet – Kittle angle ($\alpha_{Y\text{-}K}$) and is calculated using Eq. (6). The calculated values of $\boldsymbol{\alpha_{Y\text{-}K}}$ are ranging between 60 and 70°. The values of $\alpha_{Y\text{-}K}$ of the sample with increasing Sm^{3+}–Gd^{3+} concentration was found to increase. This increase in $\alpha_{Y\text{-}K}$ suggests that there is increasing tendency for triangular spin arrangement on the B- site which results in decreased A-B exchange interaction. The values of M_r, M_s, H_c, n_B, and $\boldsymbol{\alpha_{Y\text{-}K}}$ are listed in Table 3.

4.6. Electron paramagnetic resonance

In polycrystalline ferrites, losses are associated with defects and the anisotropy field distribution, and with electrical conduction a common problem, especially in spinels, is the presence of Fe^{2+}, which promotes a hopping conduction process in combination with Fe^{3+}. The physical origin of losses in polycrystalline ferrites, through its effects on the line width, has been recently investigated in detail; the dominant role of grain boundaries is apparent [42,43]. As Sm–Gd content increases the intensity of the signal decreased (Fig. 7). It is clear from the spectra that the broadness of the EPR spectra increases with the increase in Sm–Gd ion concentration, which is due to the increase in relaxation time. The *g* values were analysed using Lorentzian distribution function and it is given in Table 3. The spectra of these samples show a single broad signal with a very weak hump, indicating the presence of isolated Fe^{3+} and Sm^{3+}–Gd^{3+} ions of a *g*-value about 4.3. The g value for the superexchange coupled pair between Fe^{3+} and Sm–Gd ((Fe^{3+}-O-(Sm^{3+}–Gd^{3+}))) would be approximately 2.20 because the spectrum for Sm^{3+}–Gd^{3+} ions normally give a g value in the range 2.2–2.3, and for Fe^{3+} it generally gives 2.0. The spectrum of the Fe^{3+} coupled pair (Fe^{3+}-O-Fe^{3+}) is known to give a line with $g = 2.0$. So, the effective value obtained, $g = 2.10$, seems to favour the Fe^{3+}-O-(Sm^{3+}–Gd^{3+}) rather than the Fe^{3+}-O-Fe^{3+}. In these nanomagnetic Sm^{3+}–Gd^{3+} substituted MnZn ferrites *g* value decreases with increase in Sm^{3+}–Gd^{3+} content, which exhibits the strengthening of magnetic moment with Sm^{3+}–Gd^{3+} substitution and decrease in super exchange interaction among cations through oxygen. This decrease is due to the isotropic alignment of magnetic moments with the increase in samarium gadolinium ion concentration [44]. Based on the g values we can confirm that these ferrites are showing strong EPR signal and narrow signal is mainly due to superexchange interaction between Sm^{3+}–$Gd^{3+}$and Fe^{3+} ions. It is found that the peak-to-peak amplitude and the point of minimum derivative (H_0 = 3758Oe) remain nearly the same in all samples; however, the point of maximum derivative shifts toward the lower applied magnetic field with the increase in Sm^{3+}–Gd^{3+} ion concentration. In these samarium gadolinium substituted Mn–Zn ferrite samples, the *g*-value decreases with the increase of Sm^{3+}–Gd^{3+} ion concentration. And the values are comparable with reported values [45].

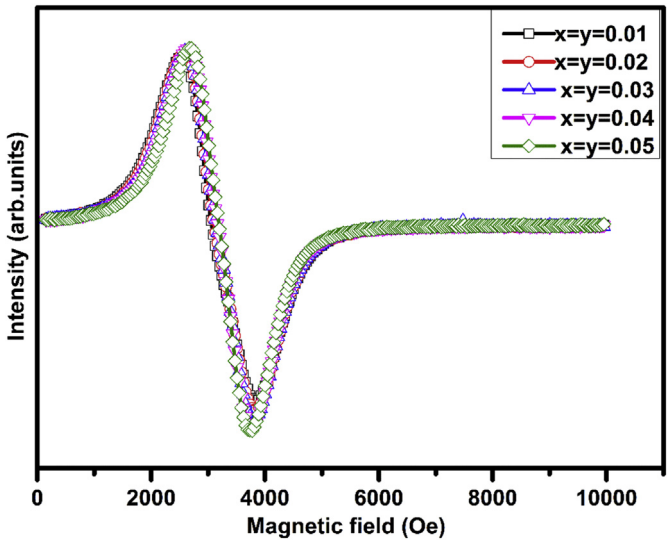

Fig. 7. EPR spectra of $Mn_{0.4}Zn_{0.6}Sm_xGd_yFe_{2-(x+y)}O_4$ samples with (x = y = 0.01, 0.02, 0.03, 0.04 and 0.05).

5. Conclusions

The XRD patterns of $Mn_{0.4}Zn_{0.6}Sm_xGd_yFe_{2-(x+y)}O_4$ ($x = y = 0.01$, 0.02, 0.03, 0.04 and 0.05) nanoparticles confirm the cubic spinel structure with the appearance of small peaks represent secondary phases i.e Fe_2O_3, $SmFeO_3$ and $GdFeO_3$ phases. The spin resonance reveals the increase in line width, line intensity in spin concentration with Sm^{3+}-Gd^{3+} ions and the *g* values decreases with increase in concentration. The saturation magnetization, remnant and decrease with increase of Sm^{3+}-Gd^{3+} ions into MnZn ferrite. This decrease is due to the occupancy of Sm^{3+}-Gd^{3+} ions replacingFe^{3+} ions at the octahedral sites, which leads to the dipole–dipole interaction. The low values of dielectric constant and high dielectric loss, magnetic properties and broad distribution of EPR line width of these ceramics are opening thereal opportunity to use them for microwave devices i.e L band (1–2 GHz) military telemetry, GPS, mobile phones (GSM), amateur radio and S band (2–4 GHz) weather radar, surface ship radar, and some communications satellites (microwave ovens, microwave devices/communications, radio astronomy, mobile phones, wireless LAN, Bluetooth, ZigBee, GPS, amateur radio).

Acknowledegments

The Author (V. Jagadeesha Angadi) are thankful to the UGC, New Delhi for giving financial support through the Major Research project.

References

[1] M. Zheng, X.C. Wu, B.S. Zou, Y.J. Wang, J. Magn. Magn. Mater 183 (1998) 152.
[2] A.C.F.M. Costa, E. Tortella, M.R. Morelli, R.H.G.A. Kiminami, J. Magn. Magn. Mater. 256 (2003) 174.
[3] A. Verma, T.C. Goel, R.G. Mendiratta, M.I. Alam, Mater. Sci. Eng. B60 (1999) 156.
[4] N. Rezlescu, E. Rezlescu, D.P. Popa, L. Rezlescu, J. Alloys Comp. 275–277 (1998) 657.
[5] R. Islam, M.A. Hakim, M.O. Rahman, H. Narayan Das, M.A. Mamun, J. Alloys Compd. 559 (2013) 174–180.
[6] Ashok Kumar, et al., Ceram. Int. 41 (2015) 1297–1302.
[7] K. Praveena, K. Sadhana, S. Srinath, S.R. Murthy, Mater. Res. Innov. 18 (1) (2014) 69–75.
[8] K. Praveena, B. Radhika, S. Srintah, AIP Conf. Proc. 1447 (2012) 289.
[9] K. Praveena, S. Srinath, Adv. Sci. Eng. Med. 6 (3) (2014) 359–365.
[10] K. Praveena, K.B.R. Varma, J. Mater. Sci. Mater. Electron. 25 (2014) 3103–3108.
[11] J.F. Wang, C.B. Ponton, I.R. Harris, J. Magn. Magn. Mater 298 (2006) 122.
[12] K. Sadhana, R. Sandhya, S.R. Murthy, K. Praveena, Mater. Focus 3 (4) (2014) 291–299.
[13] K. Praveena, K.B.R. Varma, J. Mater. Sci. Mater. Electron. 25 (1) (2014) 111–116.
[14] K. Praveena, S. Srinath, J. Magn. Magn. Mater. 349 (2014) 45–50.
[15] C.H. Chen, M.H.J. Emond, E.M. Kelder, B. Meester, J. Schoonman, J. Aerosol Sci. 30 (7) (1999) 959.
[16] A. Thakur, M. Singh, Ceram. Inter 29 (2003) 505.
[17] Chemistry of Nanocrystaline Oxide Materials, Combustion Synthesis, Properties and Applications, K.C. Patil, M.S. Hegde, Tanu Rattan and S.T. Aruna, world scientific publisher.
[18] J. Rodriguez-Carvajal, FULLPROF: a program for rietveld refinement and pattern matching analysis, in: Abstracts of the Satellite Meeting on Powder Diffraction of the XV Congress of the IUCr, 1990, p. 127. Toulouse, France.
[19] B.J. Madhu, V. JagadeeshaAngadi, H. Mallikarjuna, S.O. Manjunatha, B. Shruthi, R. Madhu Kumar, Adv. Mater. Res. 584 (2012) 299–302.
[20] G.K. Williamson, W.H. Hall, Acta Metall. 1 (1953) 22–31.
[21] V.G. Patil, Sagar. E. Shirsath, S.D. More, S.J. Shukla, K.M. Jadhav, J. Alloys Compd. 488 (2009) 199–220.
[22] S. Giri, S. Samanta, S. Ganguli, A. Bhumik, J. Magn. Mater 285 (2005) 296–302.
[23] M. Ishil, M. Nakahita, Yamanka, J. Solid State Commun. 11 (1972) 209.
[24] O.M. Hemeda, J. Magn. Magn. Mat. 281 (2004) 36.
[25] M.A. EL Hiti, A.I. El Shora, Seoud S.M. Hammed, Phase Trans. 56 (1995) 35.
[26] V.A. Halfner, N.D. Zverev, V.P. Romanov, Phys. Stat. Sol. A 12 (1975) 623.
[27] E. Melagiriyappa, H.S. Jayanna, J. Alloys Compd. 482 (2009) 147–150.
[28] A.B. Gadkari, T.J. Shinde, P.N. Vasambekar, Mater. Charact. 60 (11) (2009) 1328–1333.
[29] Jie Song, Lixi Wang, Naicen Xu, Qitu Zhang, J. Rare Earths 28 (3) (2010) 451.
[30] L.L. Hench, J.K. West, Principles of Electronic Ceramics, Wiley, New York, 1990, p. 189.
[31] A.M. Shaikh, S.S. Bellad, B.K. Chougule, J. Magn. Magn. Mater 195 (2) (1999) 384–390.
[32] John Jacob, M. AbdulKhadar, Anil Lonappan, K.T. Mathew, Bull. Mater. Sci. 31 (2008) 847–851.
[33] K. Iwauchi, Jpn. J. Appl. Phys. 10 (1971) 152.
[34] L.G. Van Uitert, Proc. IRE 44 (1956) 1294.
[35] S. Sangeeta Thakur, C. Katyal, M. Singh, J. Magn. Magn. Mater 321 (2009) 1.
[36] Thankachan Smitha, P. Binu, Sheena Xavier Jacob, E.M. Mohammed, J. Mag. Mag. Mat. 348 (2013) 140–145.
[37] S. Chakraverty, M. Bandyopadhyay, J. Phys. Condens. Matter 19 (2007) 16, 216201.
[38] L. Neel, Proc. Phys. Soc. Lond. A 65 (1952) 869.
[39] I.M. Obaidat, J.S. Kouvel, Y. Huang, G. Friedman, J. Magn. Magn. Mater 223 (2001) 88.
[40] J. M. Hastings and L. M. Corliss, Rev. Mod. Phys. 25, 114.
[41] Jagdish Chand, Satish Verma, M. Singh, J. Alloys Compd. 552 (2013) 264–268.
[42] N. Mo, Y.Y. Song, C.E. Patton, J. Appl. Phys. 97 (2005) 1.
[43] N. Mo, J.J. Green, P. Krivosik, C.E. Patton, J. Appl. Phys. 101 (2007) 023914.
[44] R. Massart, D. Zins, F. Gendron, J. Magn. Magn. Mater 201 (1999) 73.
[45] A. Kumar, M.S. Yadav, Magnetohydrodynamics 49 (2013) 191.